Transmissive RIS for B5G Communications: Design, Prototyping, and Experimental Demonstrations

Junwen Tang, Mingyao Cui, Shenheng Xu, *Member, IEEE*, Linglong Dai, *Fellow, IEEE*, Fan Yang, *Fellow, IEEE*, and Maokun Li, *Senior Member, IEEE*

***Abstract*— Reconfigurable intelligent surface (RIS) has been widely considered as a key technique to improve spectral efficiency for the 5th generation (5G) and beyond 5G (B5G) communications. Compared with most existing research that only focuses on the reflective RIS, the design and prototyping of a novel transmissive RIS are presented in this paper, and its enhancement to the RIS-aided communication system is experimentally demonstrated. The 2-bit transmissive RIS element utilizes the penetration structure, which combines a 1-bit current reversible dipole and a 90° digital phase shifter based on a quadrature hybrid coupler. A transmissive RIS prototype with 16 × 16 elements is designed, fabricated, and measured to verify the proposed design. The measured phase shift and insertion loss of the RIS element validate the 2-bit phase modulation capability. Being illuminated by a horn feed, the prototype achieves a maximum broadside gain of 22.0 dBi at 27 GHz, and the two-dimensional beamforming capability with scan angles up to ±60° is validated. The experimental results of the RIS-aided communication system verify that by introducing the extra gain and beam steering capability, the transmissive RIS is able to achieve a higher data rate, reduce the transmit power, improve the transmission capability through obstacles, and dynamically adapt to the signal propagation direction.**

***Index Terms*— Transmissive RIS, 2-bit phase shifter, prototyping.**

I. Introduction

With the ever-growing demands on system capacity from the first generation (1G) to 5G, efficiently exploiting spatial resources via advanced array technologies has always been an hotspot [2], [3]. Recently, reconfigurable intelligent surface (RIS) has attracted great attention for its capability of making full use of spatial resources and improving spectral efficiency by smartly manipulating electromagnetic (EM) environments [4]. Specifically, a RIS is usually built on hundreds or even thousands of passive elements, which is generally employed between the user equipment (UE) and base station (BS) to establish an extra reflecting link. Given that the phase states of a RIS's elements could be intelligently reconfigured to form arbitrary beam shapes with low cost and low power, RISs have abundant virtues on network coverage extension, capacity enhancement, power saving, and interference cancellation in the beyond 5G (B5G) networks. Therefore, a large number of signal processing techniques and experiments have been implemented to demonstrate the superiority of RIS [4], [5], [6], [7], [8].

Nevertheless, existing research contributions mainly consider the employment of reflective RIS [4], [5], [6], [7], [8], which may result in undesired coverage holes in a cell and unluckly limits the application of RIS. Specifically, for reflective RIS, the base station and user need to be located on the same side of the RIS, which brings extra geographical constraints on the physical topology [9]. For instance, reflective RIS is difficult to assist communication between a transmitter outside a vehicle and a receiver inside it. To cope with this problem, the concept of transmissive RIS is attracting growing attentions [10]. Rather than being reflected, signals can transmit through a transmissive RIS to form directional beams. In this way, transmissive RIS can potentially fill in the coverage holes of reflective RIS. It should be mentioned that in the literature, transmissive RIS has also been given some similar terminologies, such as transmittarray and intelligent transparent surface [9].

The phase reconfigurability is the most essential capability for a transmissive RIS. Solid-state electronic devices are commonly integrated in each constituent RIS element to dynamically control its phase response. Continuous phase shifts can be realized using analog-type devices like varactor diodes [10], [11], [12], [13], [14], [15], [16], [17]. The phase shift range usually exceeds 360° so that the phase errors are negligible. However, the transmissive RIS has a very high transmission insertion loss, which can be up to 5.7 dB [13]. As a consequence, the aperture efficiency of the RIS is considerably reduced. At high frequencies, switch-type devices are widely used to produce discrete phase shifts,

Manuscript received 28 February 2023; revised 20 June 2023; accepted 21 June 2023. Date of publication 10 July 2023; date of current version 20 November 2023. This work was supported in part by the National Natural Science Foundation of China under Grant U2141233 and in part by the National Key Research and Development Program of China under Grant 2020YB1807201. An earlier version of this paper was presented in part at the 2020 IEEE International Symposium on Antennas and Propagation and North American Radio Science Meeting [DOI: 10.1109/IEEECONF35879.2020.9330153]. The associate editor coordinating the review of this article and approving it for publication was A. El Shafie. *(Corresponding author: Shenheng Xu.)*

Junwen Tang is with the Aerospace Information Research Institute, Chinese Academy of Sciences, Beijing 100094, China (e-mail: tjw17@tsinghua.org.cn).

Mingyao Cui, Shenheng Xu, Linglong Dai, Fan Yang, and Maokun Li are with the Department of Electronic Engineering, Tsinghua University, Beijing 100084, China (e-mail: cui-my16@tsinghua.org.cn; shxu@tsinghua.edu.cn; daill@tsinghua.edu.cn; fan_yang@tsinghua.edu.cn; maokunli@tsinghua.edu.cn).

Color versions of one or more figures in this article are available at https://doi.org/10.1109/TCOMM.2023.3292477.

Digital Object Identifier 10.1109/TCOMM.2023.3292477

including p-i-n diodes, Radio-Frequency (RF) Micro-Electro-Mechanical System (MEMS) switches, and etc [13], [14], [15], [16], [17]. Most existing designs focus on 1-bit phase reconfigurability, where the design and fabrication difficulties are manageable [18], [19], [20], [21], [22], [23], [24], [25], [26]. For example, a classic design of an O-slot patch loaded with two positive-intrinsic-negative (p-i-n) diodes in [18] adopted the current reversal mechanism to realize a stable 180° phase shift in a wide frequency band. The minimum measured insertion loss is 1.7/1.9 dB at 9.8 GHz. Several other attempts were made to obtain a 2-bit phase resolution [27], [28]. Specifically, a monolithically fabricated 2-bit prototype using MEMS switches [27] was able to produce 4 phase states, but the measured insertion loss is 4.2–9.2 dB at Ka band. A compact 2-bit element using a modified O-slot patch [28] was designed, fabricated and measured. The measured insertion loss is 1.5–2.3 dB at 29.0 GHz, and the measured 3-dB transmission bandwidth is 10.1–12.1% for four phase states.

The phase quantization errors associated with discrete phase shifts inevitably introduce performance degradation [29], [30], [31]. It is observed that the 1-bit element designs suffer from 3–4 dB insertion loss attributed to the coarse phase resolution, which results in a low aperture efficiency. The sidelobe levels are significantly higher, sometimes even causing unwanted grating lobes. By contrast, 2-bit designs are considered a well-balanced choice between the element performance and the design complexity. The phase quantization loss can be greatly reduced to less than 1 dB, and the sidelobe envelop can be significantly improved as well.

Nonetheless, there are only a few 2-bit designs in the literature. One of the important reasons is that, compared to 1-bit designs, more transition structures and electronic devices are needed to achieve four stable phase states. The conventional design approach solely relies on the two-dimensional unit-cell footprint because of the printed-circuit board (PCB) fabrication process. It becomes extremely challenging to lay out a variety of constituent element parts in a greatly limited sub-wavelength array grid. Consequently, more numbers of stacked layers are used, which results in the higher fabrication complexity and cost. To the best of our knowledge, the design, fabrication, and measurement of the 2-bit transmissive RIS have not been well studied.

In this paper, the 2.5-D penetration structure [32] is exploited to make the best of the longitudinal space in the propagation direction to develop the 2-bit transmissive RIS. Specifically, our contributions are summarized below.

- Firstly, a 90° digital phase shifter is proposed and realized using two p-i-n diodes based on a quadrature hybrid coupler [33]. Combined with a 1-bit current reversible dipole, 2-bit phase resolution is achieved at the millimeter wave (mmWave) band. In addition to some preliminary results reported in the authors' conference paper [1], the 2-bit RIS element is further optimized and more detailed analysis is presented in this journal paper.
- Furthermore, a prototype with 16 × 16 RIS elements and a logic circuit control board is fabricated and measured. The measured results show that the prototype can achieve a maximum broadside gain of 22.0 dBi at 27 GHz, with the corresponding aperture efficiency of 25.3%. Moreover, the measured radiation performances for scan angles are presented as well, demonstrating the beamsteering capability in a large angle up to 60°.
- Finally, a transmissive RIS-aided mmWave wireless communication prototype is developed to demonstrate the performance of the fabricated 2-bit transmissive RIS. The experimental results verify that the 2-bit transmissive RIS can achieve a higher data rate, reduce the transmit power, improve the transmission capability through obstacles, and dynamically adapt to the signal propagation direction.

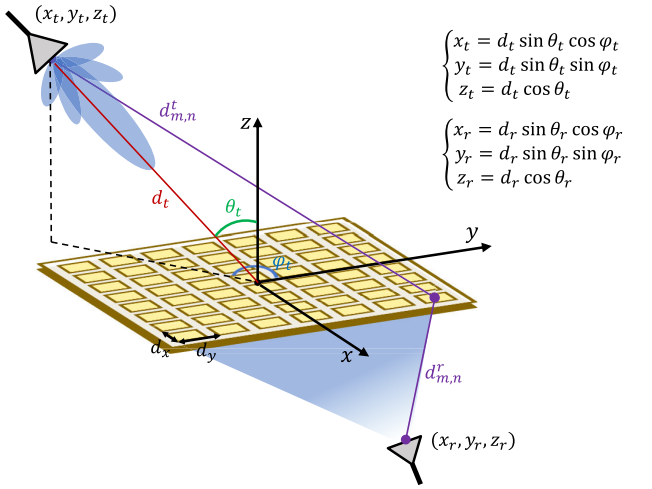

Fig. 1. System model of transmissive RIS-aided communication systems.

Organization: The reminder of this paper is organized as follows. The communication model of transmissive RIS is introduced in Section II. Then, in Section III, we describe the structure and simulated performance of the element of the designed transmissive RIS. Section IV provides the experimental results for the 16 × 16 elements RIS prototype in the microwave anechoic chamber. A transmissive RIS-aided wireless communication prototype is set up to further measure the performance of the proposed RIS in Section V. Finally in Section VI, conclusions are drawn.

II. System Model

In this section, we describe the system model of the transmissive RIS-aided communication system.

A. System Model

We consider that the transmitter (Tx) employs a horn antenna to communicate with a single-antenna receiver (Rx), where an N-element transmissive RIS is used for enhancing the signal power. As shown in Fig. 1, the RIS is a uniformly planar array (UPA) placed in the x-y plane, and its geometric center is located at the origin of the coordinate system. Let N_x denote the number of antennas on the row and N_y denote the number of antennas on the column, with $N = N_x N_y$. The antenna spacing along the x axis and y axis are d_x and d_y respectively, which are usually half of the wavelength. The coordinates of the Tx and Rx are (x_t, y_t, z_t) and (x_r, y_r, z_r). The coordinate of the (m, n)-th antenna in the m-th row and n-th column of the RIS is $(\delta_m d_x, \delta_n d_y, 0)$, where $\delta_m = m - (N_x - 1)/2$ and $\delta_n = n - (N_y - 1)/2$

with $m \in \{0, 1, \cdots, N_x - 1\}$ and $n \in \{0, 1, \cdots, N_y - 1\}$. We use the symbols d_t, θ_t, and φ_t to denote the distance, the azimuth angle, and the elevation angle between the center of the RIS and the Tx. The relationship between (x_t, y_t, z_t) and $(d_t, \theta_t, \varphi_t)$ is shown in Fig. 1. Similarly, we use the symbols d_r, θ_r, and φ_r to denote the distance, the azimuth angle, and the elevation angle between the center of the RIS and the Rx, where the relationship between (x_r, y_r, z_r) and $(d_r, \theta_r, \varphi_r)$ is shown in Fig. 1 as well.

We denote $\mathbf{f} \in \mathbb{C}^{N\times 1}$ as the Tx-RIS channel, and denote $\mathbf{g} \in \mathbb{C}^{N\times 1}$ as the RIS-Rx channel. Since this paper aims to evaluate the function of the transmissive RIS, the direct link between the Tx and Rx is ignored in this paper. Denote $[\mathbf{g}]_{m,n}$ and $[\mathbf{f}]_{m,n}$ as the channel from the (m, n)-th antenna of the RIS to the Rx and Tx, respectively. Then, the free space channel model is adopted to represent $[\mathbf{g}]_{m,n}$ and $[\mathbf{f}]_{m,n}$ as [4]

$$[\mathbf{g}]_{m,n} = \sqrt{\frac{\lambda G_g F_g(\theta_r, \varphi_r)}{4\pi}} \frac{e^{-j\frac{2\pi}{\lambda} d^r_{m,n}}}{d^r_{m,n}}, \tag{1}$$

$$[\mathbf{f}]_{m,n} = \sqrt{\frac{\lambda G_f F_f(\theta_t, \varphi_t)}{4\pi}} \frac{e^{-j\frac{2\pi}{\lambda} d^t_{m,n}}}{d^t_{m,n}}, \tag{2}$$

where λ represents the wavelength, $d^r_{m,n}$ and $d^t_{m,n}$ denote the distance from the (m, n)-th antenna of the RIS to the Rx and Tx, respectively. Moreover, G_g and $F_g(\theta_r, \varphi_r)$ denote the antenna gain and the normalized power radiation pattern of the side of RIS facing the receiver, while G_f and $F_f(\theta_t, \varphi_t)$ correspond to those of the side of RIS facing the transmitter [4].

Let s denote the transmitted symbol with $\|s\|_2 = 1$. We use symbols G_t, F_t, P_t, G_r, F_r to represent the transmitter antenna gain, the transmit power, the normalized radiation power of the transmitter, the receiver antenna gain, and the normalized radiation power of the receiver. Denote $w \sim \mathcal{CN}(0, \sigma^2)$ as the additive Guassian noise with variance σ^2. Then the noised received signal by the Rx can be modeled as

$$\begin{aligned} y &= \sqrt{P_t} \sum_{m=0}^{N_x-1} \sum_{n=0}^{N_y-1} [\mathbf{g}]_{m,n} [\mathbf{f}]_{m,n} \Gamma e^{j\phi_{m,n}} s + w, \\ &= \frac{\lambda \Gamma \sqrt{P_t G F}}{4\pi} \sum_{m=0}^{N_x-1} \sum_{n=0}^{N_y-1} \frac{1}{d^t_{m,n} d^r_{m,n}} e^{j\left(\phi_{m,n} - \frac{d^t_{m,n}+d^r_{m,n}}{\lambda}\right)} s \\ &\quad + w, \end{aligned} \tag{3}$$

where $\Gamma \in [0, 1]$ is transmission loss of the (m, n)-th antenna of the RIS, $\phi_{m,n} \in [0, 2\pi]$ denotes the phase shift of the (m, n)-th antenna of the RIS, $G = G_t G_f G_g G_r$, and $F = F_t F_f(\theta_r, \varphi_r) F_g(\theta_r, \varphi_r) F_r$.

B. Beamforming for the Transmissive RIS

For the desired receiver, the transmissive RIS is designed for maximizing the received signal energy through beamforming. The received signal-to-noise ratio (SNR) can be presented as

$$\text{SNR} = \frac{P_t G F \lambda^2 \Gamma^2}{16\pi^2 \sigma^2} \left| \sum_{m=0}^{N_x-1} \sum_{n=0}^{N_y-1} \frac{1}{d^t_{m,n} d^r_{m,n}} e^{j\left(\phi_{m,n} - \frac{d^t_{m,n}+d^r_{m,n}}{\lambda}\right)} \right|^2. \tag{4}$$

To maximize SNR, it is obvious that the optimal $\phi_{m,n}$ is

$$\bar{\phi}_{m,n} = \mod\left(C + \frac{d^t_{m,n} + d^r_{m,n}}{\lambda}, 2\pi\right), \tag{5}$$

where $\mod(\cdot)$ is the mod function guaranteeing that the phase shift $\bar{\phi}_{m,n}$ is belonging to $[0, 2\pi]$ and C is an arbitrary constant. The detailed proof is provided in Appendix A. From (5), the phase shift $\phi_{m,n}$ can be obtained according to $d^t_{m,n}$ and $d^r_{m,n}$. According to the geometry relationship, $d^t_{m,n}$ and $d^r_{m,n}$ can be represented as

$$d^r_{m,n} = \sqrt{(x_r - \delta_m d_x)^2 + (y_r - \delta_n d_y)^2 + z_r^2}, \tag{6}$$

$$d^t_{m,n} = \sqrt{(x_t - \delta_m d_x)^2 + (y_t - \delta_n d_y)^2 + z_t^2}. \tag{7}$$

Therefore, the optimal solution to $\phi_{m,n}$ can be obtained accordingly. Then, for practical implementation of RIS, the limited resolution of the phase shift has to be considered. If there are b bits for quantized phase shifter, then the feasible set of phase shift is

$$\mathbf{\Phi}_b = \left\{0, \frac{1}{2^{b-1}}\pi, \cdots, \frac{2^b - 1}{2^{b-1}}\pi\right\}. \tag{8}$$

Denote the quantized phase shift as $\tilde{\phi}_{m,n}$. We meticulously configure $\tilde{\phi}_{m,n}$ to maximize the received SNR so as to enhance the communication quality, which can be formulated as the following discrete optimation problem:

$$\begin{aligned} (P_0) \max \quad & \left| \sum_{m=0}^{N_x-1} \sum_{n=0}^{N_y-1} h_{m,n} e^{j\tilde{\phi}_{m,n}} \right|^2, \\ s.t. \quad & \tilde{\phi}_{m,n} \in \mathbf{\Phi}_b, \forall (m, n) \end{aligned} \tag{9}$$

Here we denote $h_{m,n} = |h_{m,n}| e^{\angle h_{m,n}} = \frac{1}{d^t_{m,n} d^r_{m,n}} e^{-j\frac{d^t_{m,n}+d^r_{m,n}}{\lambda}}$. In our prototyping, the channel state information $h_{m,n}$ is acquired by measuring the geometry of Tx, Rx, and RIS in advance, and beamforming is performed by solving the optimization problem (P_0) with known $h_{m,n}$, which is enough for us to verify the beamforming capability of transmissive RIS. Before going ahead, it is worth mentioning that the CSI acquisition methods for estimating $h_{m,n}$ have been well studied in the literature. For example, an alternating least square algorithm was studied in [34]. Compressed sensing based algorithms exploiting the sparsity of RIS channel is studied in [35]. Besides, codebook-based beam training algorithm can also be adopted to acquire CSI [36]. The above algorithms and signaling procedure are widely adopted in reflective RIS systems. Since the system mathematical model between reflective RIS and transmissive RIS is pretty similar, these methods can be easily applied in transmissive RIS systems as well.

Now, we focus on the beamforming design problem (P_0). Since the discrete optimation problem (P_0) is non-convex and NP-hard, obtaining its global optimum requires prohibitive time complexity in the order of $\mathcal{O}(2^{Nb})$. In the literature, some discrete optimation algorithms have been proposed to find near-optimal solutions to problems similar to (P_0) with acceptable time complexity. In this article, we compare the

performance of these algorithms in low-resolution beamforming and use the best one in our prototyping. The compared algorithms are shown below.

- The hard quantization method: This method directely choose a feasible quantized phase shift $\tilde{\phi}_{m,n}$ closest to the optimal continuous phase shift $\bar{\phi}_{m,n}$, where

$$\tilde{\phi}_{m,n} = \arg\min_{\phi \in \mathbf{\Phi}_b} |\phi - \bar{\phi}_{m,n}|. \tag{10}$$

- The cross-entropy (CE) algorithm [37]: This algorithm can be regarded as a probabilistic model-based approach to solve discrete optimization problems. It assigns a specific probability distribution to the discrete phase states of each phase shifter. Then, the CE algorithm iteratively updates these probability distributions by minimizing the cross-entropy, and finally generates the phase states with the highest probability for beamforming.
- The quantum-inspired evolutionary algorithm (QEA) [38]: Rather than a quantum algorithm, QEA is actually an advanced evolutionary algorithm (EA) for discrete optimization problems. QEA introduces the concepts of quantum states, quantum gates, probability amplitude, and so forth into EA. QEA can achieve better performance in discrete optimization problems than conventional EAs, so we use it to solve the RIS beamforming problem (P_0).
- The alternating optimization (AO) algorithm [39]: This discrete phase-shift optimization algorithm is proposed for the reflective RIS. Due to the similarity of mathmatical model between reflective RIS and tranmissive RIS, we can use this algorithm to solve problem (P_0). The key idea of AO algorithm is to alternately optimize one phase shift while fixing the other $N-1$ phase shifts in an iterative manner. Specifically, for the (p,q)-th phase shift $\tilde{\phi}_{p,q}$, by fixing the other phase shifts $\tilde{\phi}_{m,n}$, $\forall (m,n) \neq (p,q)$, the optimal $\tilde{\phi}_{p,q}$ is given by

$$\tilde{\phi}_{p,q} = \arg\max_{\phi \in \mathbf{\Phi}_b} \left| h_{p,q} e^{j\phi} + \sum_{(m,n)\neq(p,q)} h_{m,n} e^{j\tilde{\phi}_{m,n}} \right|^2. \tag{11}$$

  Obtaining the optimal $\tilde{\phi}_{p,q}$ from (11) is time efficient. By repeatedly solving (11) in the order from $(p,q) = (0,0)$ to $(p,q) = (N_x-1, N_y-1)$, the objective function of (P_0) is non-decreasing. After convergence, we can arrive at a near-optimal solution of the discrete phase shifts.

We compare the achieved beam pattern of these four methods in Fig. 2. As our fabricated array has 2-bit resolution (4 phase states), we set $b = 2$ in this simulation. The other parameters are as follows: $N_x = N_y = 16$, $\lambda = 10.7$ mm, $\theta_r = \varphi_r = 0$, $d_r = 50$ mm, $\theta_r = \varphi_t = \pi/3$, $d_t = 5$ m. The dotted line denotes the beam pattern generated by the ideal continuous beamforming. Here, the beamforming gain is calculated by $\frac{\left|\sum_m \sum_n h_{m,n} e^{j\tilde{\phi}_{m,n}}\right|^2}{\left|\sum_m \sum_n |h_{m,n}|\right|^2}$. It is clear from Fig. 2

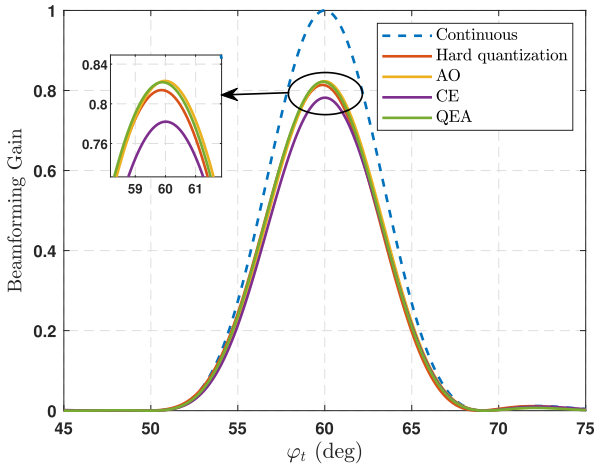

Fig. 2. Normalized beamforming gain with respect to φ_t.

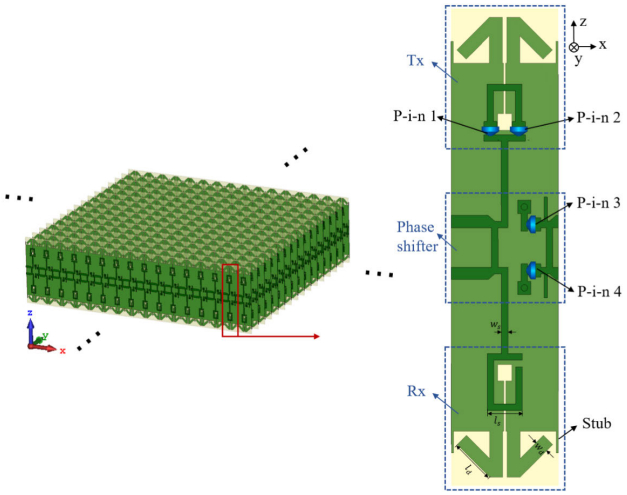

Fig. 3. Proposed 2.5-D structure of the transmissive RIS for mmWave communications.

that for a 2-bit resolution transmissive RIS, the AO and QE algorithms are slighly better than the hard quantization scheme, where more than 80% beamforming gain of the continuous beamforming is achievable. Moreover, we can find that the performance of 2-bit hard quantization is pretty close to the AO and QE algorithms. A similar conclusion was also obtained in [39]. This fact further emphasizes the importance of the fabrication of transmissive RIS with more than 2-bit resolution. As a consequence, in our prototyping, we will perform the best AO algorithm to compute the phase states of RIS. In the following sections, we will elaborate on the proposed transmissive RIS design in our communication system.

III. Proposed RIS Element Design

We describe the proposed transmissive RIS element in this section, including element design, 90° phase shifter exploited in the element, and element performance in simulation.

A. Element Design

Fig. 3 illustrates the proposed 2.5-D structure of the 2-bit transmissive RIS. Each RIS element consists of a number of

one-dimensional subarrays aligned in parallel. The constituent element utilizes the penetration structure, which is composed of a RIS-side Rx and a RIS-side Tx to receive and transmit the RF signals impinging on the RIS, respectively, and a microstrip transmission line to convey the signal through the RIS aperture. Instead of laying them out in the aperture plane, two vertical dipoles [40] are employed and arranged along the propagation direction to circumvent the space constraint imposed by the unit cell footprint. The slightly extended longitudinal space easily accommodates a 90° digital phase shifter between the RIS-side Rx and the RIS-side Tx. Combined with the 1-bit current reversible dipole, the 2-bit transmissive RIS element can be readily realized.

The 2.5-D structure slightly increases the aperture profile by $1 \sim 2$ wavelengths, but it is still much smaller compared with the aperture size. Especially at mmWave frequencies, the aperture profile is merely a couple of centimeters and will not considerably undermine the low profile and conformal features of the RIS. Each subarray can be easily fabricated on a single layer of substrate, thus avoiding the complicated multilayer PCB process and lowering the overall cost. It is also a remarkable fact that the $//$-type 2.5-D structure can be further developed into a $\#$-type or a Δ-type formation where two or three sets of subarrays can be arranged in the same aperture, so that the 2.5-D unit cell space can be more fully exploited for more constituent element parts. Hence, more advanced features such as dual-polar or dual-band designs can be accomplished.

The linearly incident wave propagating along the z axis is received by the passive RIS-side Rx composed of a vertical dipole. Then, the received signal is converted into a guided wave and conveyed along the microstrip transmission line. The phase shifter structure based on the quadrature hybrid coupler is employed. Instead of the varactor diodes used in the analog phase shifter design [33], it is terminated with reflection-type loads composed of two p-i-n diodes (model MADP-000907-14020) to provide a 0°/90° digital phase shift. The two loaded p-i-n diodes are always tuned at the same ON- or OFF-states, resulting in a 90° phase shift. The RIS-side Tx is similar to the RIS-side Rx, but the vertical dipole structure [40] is modified to integrate two p-i-n diodes (MADP-000907-14020) that are symmetrically placed in the feeding microstrip line. They are alternatively turned ON or OFF so that the excitation current flows in opposite directions. Consequently, the reversible current flow produces a stable 180° phase shift without significantly affecting magnitude response. Finally, the RIS-side Tx re-radiates the guided wave into the free space with four stable phase states of 0°/90°/180°/270°, and hence, the 2-bit phase resolution is obtained.

The frequency of the designed transmissive RIS element is 26.5 GHz, and the unit cell size is 4.9×4.9 mm^2. The proposed 2-bit element is printed on a single layer of Taconic TLX-8 substrate ($\epsilon_r = 2.55$, $\tan\delta = 0.0019$, $h = 0.254$ mm). The microstrip line and the 90° digital phase shifter are on the top of the substrate, while the vertical dipoles and the ground plane are arranged on the bottom of the substrate. The total profile of the element is 21.8 mm, corresponding to 1.9λ at the design frequency. The following geometrical parameters

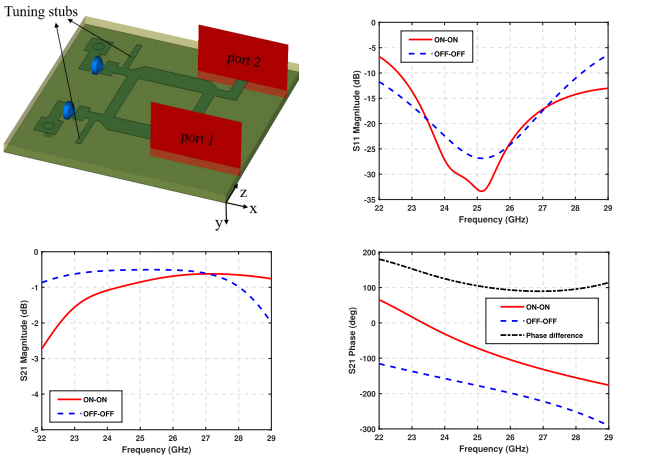

Fig. 4. Proposed 90° digital phase shifter based on a quadrature hybrid coupler: (a) the illustrative structure; (b) simulated reflection magnitude, (c) transmission magnitude, and (d) transmission phase.

are optimized after a comprehensive parametric study: $l_d = 2.1$ mm, $w_d = 0.6$ mm, $l_s = 1.6$ mm, $w_s = 0.3$ mm.

B. 90° Digital Phase Shifter

The proposed 90° digital phase shifter integrated in the 2-bit transmissive RIS element is designed to provide 0°/90° phase switching, as shown in Fig. 4 (a). It is a reflection-type phase shifter based on the quadrature coupler terminated with two reflective loads, which are composed of p-i-n diodes and short-circuited stubs. The realization of 90° phase shift is by tuning the two p-i-n diodes to work at ON-ON or OFF-OFF state, respectively. Two tuning stubs are introduced to maintain a stable desired phase shift by tuning their lengths. The digital phase shifter is modeled and simulated with a periodic boundary condition and a wave-port excitation. As can be observed from the simulation results plotted in Fig. 4 (b), a 10-dB return loss bandwidth of 22% (22.6-28.2 GHz) is achieved. Good impedance matching performance minimizes the insertion loss to less than 1 dB within the frequency band from 24.2 to 28.0 GHz. Meanwhile, from the curves plotted in Fig. 4 (d), we can find that the phase difference is close to 90° in a wide frequency band. We can conclude that the phase shifter is capable of generating desired 90° phase shift by electrically adjusting the two p-i-n diodes, thus achieving the 0°/90° digital phase switching capability with the low insertion loss.

C. Performance of the Designed Transmissive RIS Element

We simulate the proposed 2-bit RIS element with a periodic boundary condition to mimic an infinite array environment and the mutual coupling effect is also considered. The element is simulated. The simulated element performances under normal incidence for the four working states are plotted in Fig. 5. The transmission magnitude responses at 26.5 GHz are summarized in Table I. It can be seen that the average transmission insertion loss of the four states is around 1.3 dB. Moreover, the insertion losses are maintained below 3 dB ranging from 24.8 to 28.6 GHz, corresponding

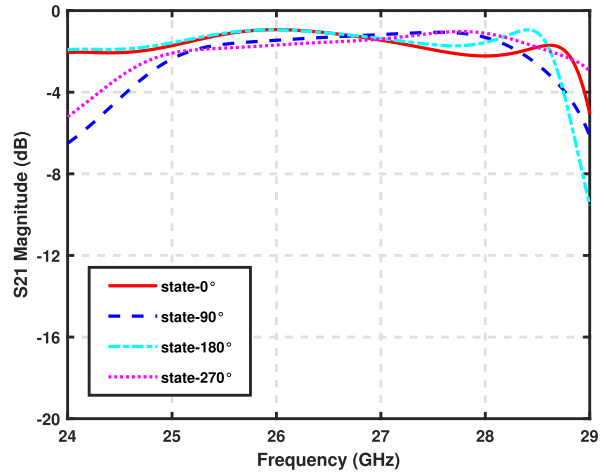

(a)

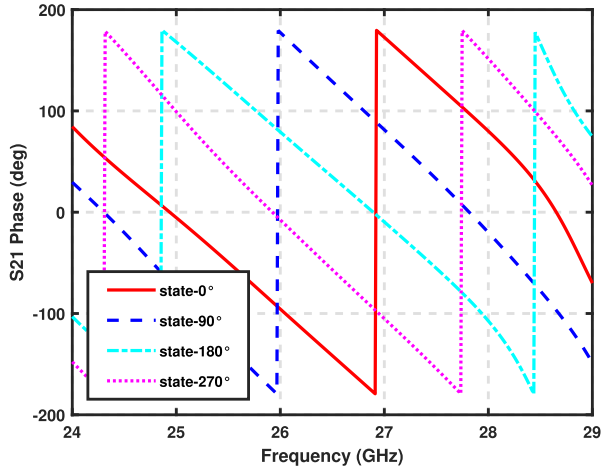

(b)

Fig. 5. Simulated transmission (a) magnitude and (b) phase of the proposed 2-bit RIS element.

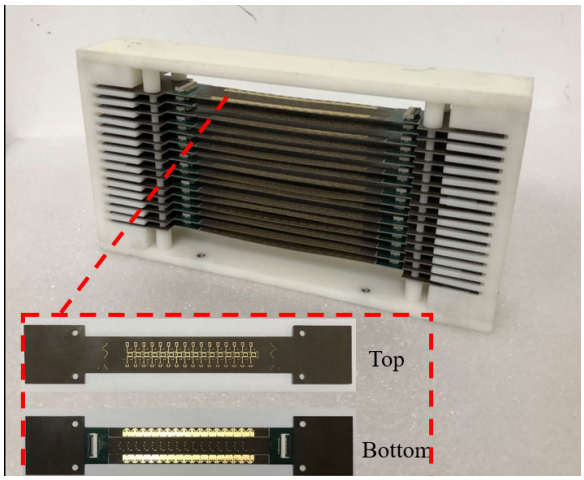

(a)

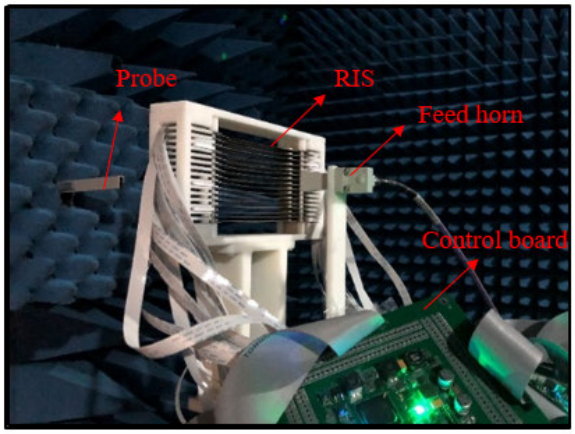

(b)

Fig. 6. Photography of (a) the fabricated transmissive RIS prototype, (b) the measurement setup in the microwave anechoic chamber.

TABLE I
SIMULATED PERFORMANCE OF THE 2-BIT RIS ELEMENT

State	Element loss @26.5 GHz	Phase shift @26.5 GHz	3-dB trans. bandwidth
1 (state-0°)	1.1 dB	-141.2°	23.6-28.9 GHz (20.1%)
2 (state-90°)	1.3 dB	-56.8°	24.8-28.6 GHz (14.2%)
3 (state-180°)	1.1 dB	34.9°	23.5-28.6 GHz (19.6%)
4 (state-270°)	1.5 dB	129.0°	24.6-29.0 GHz (16.4%)

to the 3-dB transmission bandwidth of 14.2%. The phase curves of the four states are roughly parallel with around 90° phase difference in the operating frequency band. Hence, by switching the p-i-n diodes alternatively, the RIS element successfully achieves 2-bit phase tuning capability.

IV. RIS DESIGN, FABRICATION, AND MEASUREMENT

In this section, a transmissive RIS prototype composed of 16×16 proposed elements is designed, fabricated, and measured to experimentally validate the performance of the proposed RIS element.

The photographs of the fabricated RIS prototype and the measurement setup in the microwave anechoic chamber are presented in Fig. 6. Taking advantage of the PCB technology, the RIS is easy to fabricate. The RIS is space-fed by a linearly polarized horn. The effective aperture size of the RIS prototype is 78.4×78.4 mm^2. The feeding horn illuminates the array at an optimized distance of 50 mm. To achieve the goal of phase reconfigurability, each element of the array needs to be controlled independently. There are 512 biasing lines since each element has two biasing lines to apply DC voltages to four p-i-n diodes. Two logic circuit controlling boards are attached to supply independent DC voltages of 512 channels, and they are connected to the biasing lines through several connectors.

We measure the fabricated prototype in a planar near-field anechoic chamber. From the measured performance of the broadside beam depicted in Fig. 7, a peak gain of 22.0 dBi is obtained at 27.0 GHz, which is 9.3 dB higher than that of the feeding horn. The corresponding aperture efficiency is 25.3%. The slight frequency shift to higher frequencies is mainly attributed to the tolerance in fabrication and the supporting structure. The measured radiation pattern is in good agreement with the theoretical prediction based on the array theory.

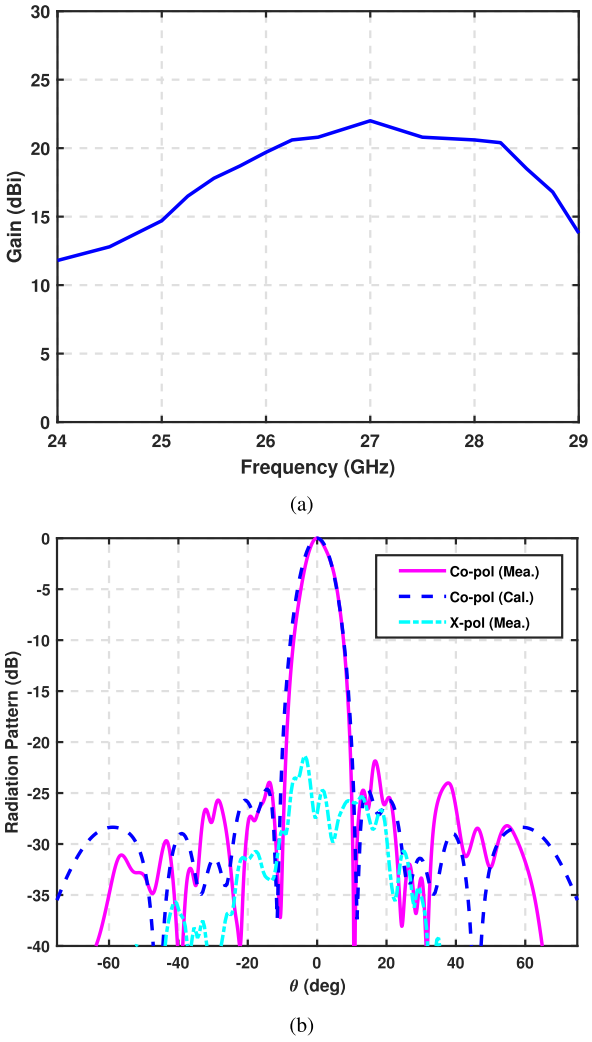

Fig. 7. Performance of the broadside beam: (a) measured gain bandwidth, (b) calculated and measured normalized radiation patterns at 27.0 GHz.

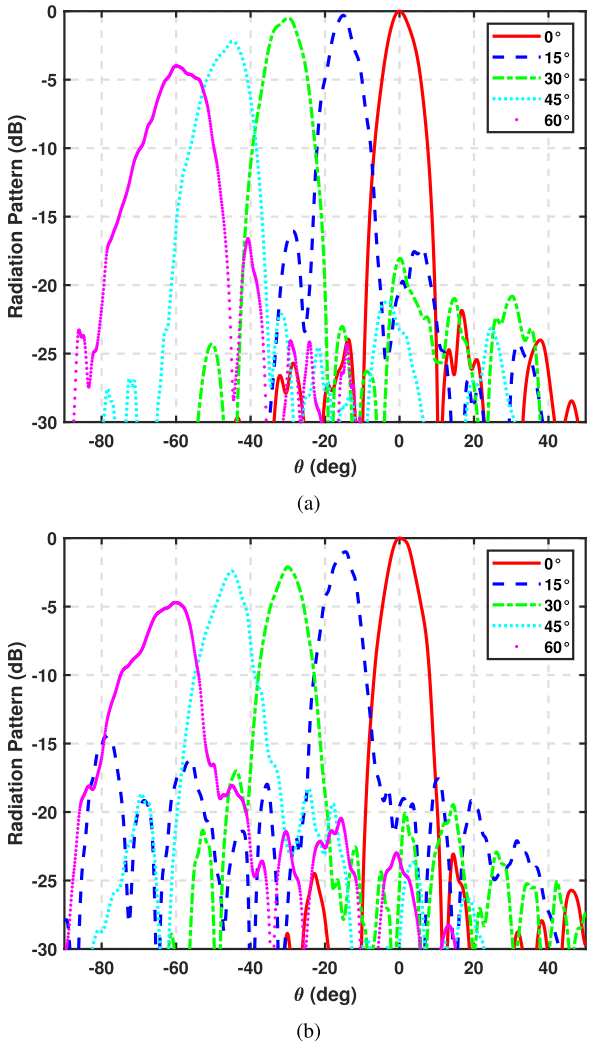

Fig. 8. Measured radiation patterns of scanned beams at 27.0 GHz in (a) E-plane, (b) H-plane.

The measured sidelobe level is below −22 dB, remarkably lower than that of the 1-bit designs, which is mainly attributed to the finer phase resolution of the 2-bit RIS. The measured cross-polarization level is −21.3 dB.

The radiation behaviors of the scanned beams are measured as well to experimentally verify the dynamic beam scanning capability of the transmissive RIS in two-dimensional space. By controlling the phase of each RIS element, the transmitted focused beam can be formed by the RIS in the given direction. As shown in Fig. 8, the measured scanned beams in the angular region from 0° to −60° show accurate beam pointing and well-defined patterns in both E-plane and H-plane. Note that the beams in the opposite angular region are omitted due to the symmetry. The measured 60° scan gain losses are 4.0 dB and 5.0 dB in two principal planes, respectively. Table II compares the performance of the proposed 2-bit RIS with other RIS designs published in literature. It is evident that this work achieves the highest aperture efficiency.

V. Transmissive RIS-Aided Wireless Communication Prototype

In this section, a transmissive RIS-aided wireless communication prototype is set up to further measure the performance of the designed transmissive RIS in practical communication scenarios.

A. Measurement Setup

As illustrated in Fig. 9, we carry out the experiment in an office environment. The prototype is composed of the transmitter side, the RIS, and the receiver side. Both the receiver and the transmitter utilize the software-defined radio (SDR) platform, composed of the PXI hardware architecture and the LabVIEW system design software, to realize transmission at the mmWave band.

The transmitter consists of the transmitter host, the FPGA, the ADC module, the mmWave upconverter, and a horn antenna. The transmitter host controls the system parameters, including modulations, the transmit power, the central frequency, and so on. A high-speed bitstream is first delivered by the host to the FPGA module. The FPGA module realizes complex signal processing, including channel coding, constellation mapping, OFDM modulation, and etc. After that, the signals are sequentially processed by the ADC and the mmWave upconverter to form mmWave analog signals suitable for transmission in wireless channels.

TABLE II
PERFORMANCE COMPARISON WITH OTHER 2-BIT TRANSMISSIVE RIS DESIGNS

Ref.	Freq. [GHz]	Tunable device	Number of tunable devices	Number of dielectric layers	Profile	3dB-gain bandwidth	Gain [dBi]	Aper. eff. [%]
[26]	34.8	MEMS	5	4	0.116λ	-	9.2	6.2
[27]	29	p-i-n	4	5	0.125λ	16.2%	19.8	15.9
Our work	27	p-i-n	4	3	1.9λ	10%	22.0	25.3

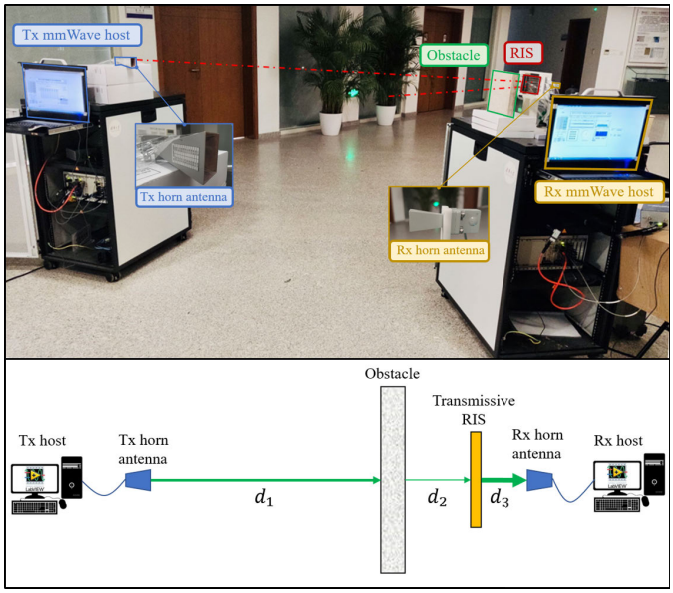

Fig. 9. Transmissive RIS-aided wireless communication prototype.

The transmissive RIS has 256 2-bit elements. It receives the signals from the transmitter, tunes the phase of received signals, and then directionally transmits them towards the receiver. Moreover, for validating that a transmissive RIS is able to overcome obstacles, we can also place an obstacle, such as a piece of marble, between the RIS and the base station.

Similar to the transmitter, the receiver is composed of the receiver host, the FPGA, a DAC module, a mmWave down converter, and a horn antenna. At the receiver side, the Rx horn antenna first receives the signal and transforms them the digital domain by the mmWave down converter and the DAC module. Then, the FPGA module is responsible for recovering the bitstream by channel estimation, OFDM demodulation, decoding, CRC check and etc. Moreover, according to the results of the CRC check, the host obtains the block error rate and calculates the data rate. Finally, the received constellation and the data rate are illustrated on the screen of the host.

In Table III, the detailed settings of our mmWave platform are provided. We consider a downlink communication scenario. The bandwidth is 800 MHz and the carrier frequency is 27.0 GHz. The horn antenna of the transmitter, the transmissive RIS, and the horn antenna of the receiver are on the same height of 1.5 m and are all horizontally polarized. A piece of marble with thickness of 0.03 m is employed to mimic the obstacle. Let d_1, d_2, and d_3 denote the distance between the Tx antenna and the obstacle, the distance between the obstacle and the RIS, the distance between the RIS and the Rx antenna. They are set as $d_1 = 2.4$ m, $d_2 = 0.2$ m, and $d_3 = 0.05$ m, respectively. The fabricated transmissive RIS works at 27.0 GHz with an additional 9.3 dB array gain when being illuminated by the Rx horn antenna. The azimuth angle and the elevation angle from the RIS center to the Tx/Rx are all zero, i.e., $\theta_t = \theta_r = \varphi_t = \varphi_r = 0^\circ$ as shown in Fig. 1. We verify the performance of this RIS in terms of array gain and data rate.

TABLE III
SYSTEM PARAMETERS

Parameters	Value	Parameters		Value
Carrier frequency	27.0 GHz	Antenna gain	Tx	22.7 dBi
System bandwidth	800 MHz		Rx	9.2 dBi
Waveform	CP-OFDM	Trans. RIS	Array gain	19.8 dBi
FFT size	2048		Frequency	27.0 GHz
Carrier spacing	75 KHz		Phase resolution	2 bit
ADC/DAC resolution	14 bit		Array size	16×16
		Tx/Rx height		1.5 m
Modulation	16-QAM	d_1		2.4 m
Coding	Turbo	d_2		0.2 m
Code rate	1/2	d_3		0.05 m

TABLE IV
ARRAY GAIN PERFORMANCE

With or without RIS	Transmit power	Data rate
×	13.6 dBm	1024 Mbps
✓	5.4 dBm	1121 Mbps

B. Array Gain Performance Assessment

To evaluate the array gain, we remove the obstacle and assess the system performance with or without the transmissive RIS. The experiment results are presented in Table IV. Specifically, without the transmissive RIS, when the transmit power reaches 13.6 dBm, the data rate can reach 1024 Mbps. By contrast, to achieve a similar transmission rate of 1121 Mbps, only 5.4 dBm transmit power is required with the help of transmissive RIS. It is obvious that the transmit power is reduced by 8.2 dB. As we measured in the anechoic chamber, the RIS can provide a 9.3 dB array gain, which is consistent with the transmit power reduction measured by our prototype. Therefore, it is obtained that the transmissive RIS-aided communication prototype can reduce the transmit power by the

TABLE V
DATA RATE PERFORMANCE

With or without RIS	With or without obstacle	Azimuth angle	Data rate
×	×	0°	1024 Mbps
✓	×	0°	1683 Mbps
×	✓	0°	0 Mbps
✓	✓	0°	1683 Mbps

TABLE VI
BEAM STEERING EVALUATION

With or without RIS	With or without obstacle	Azimuth angle	Data rate
×	×	30°	450 Mbps
✓	×	30°	1683 Mbps
×	✓	30°	0 Mbps
✓	✓	30°	1683 Mbps

magnitude close to the array gain provided by the RIS, while maintaining the similar communication performance.

C. Data Rate Assessment

To further validate that the fabricated transmissive RIS is able to overcome obstacles, we also introduce a piece of marble into the system to evaluate the data rate performance. Specifically, depending on whether the obstacle and/or the RIS exist, there are in total four communication scenarios. The transmit power is fixed to 13.6 dBm. The experiment results are tabulated in Table V. Two conclusions can be derived accordingly. One is that the fabricated RIS is able to improve the transmission data rate. When the obstacle is removed, the introduction of the transmissive RIS increases the data rate from 1024 Mbps to 1683 Mbps. It is worth mentioning that 1683 Mbps is the highest data rate that the communication prototype can support with 16-QAM modulation. The other is that the transmissive RIS is able to overcome obstacles because of the additional array gain it provides. Specifically, when the direct Tx-Rx link is blocked by the marble, data transmission is completely interrupted without the help of transmissive RIS. By contrast, the introduction of the transmissive RIS re-establishes the communication link and achieves the highest 1683 Mbps. This is because that the array gain provided by the RIS is higher than the attenuation of the obstacle.

D. Beam Steering Assessment

Finally, the beam steering ability of the fabricated transmissive array is validated in this subsection. Compared to the communication settings in previous experiments, the transmit power is fixed to 13.6 dBm and the azimuth angle from the transmissive RIS to the transmitter is $\theta_t = 30°$. The other settings are the same. The experiment results are shown in Table VI. Without the assistance of transmissive RIS, the data rate is reduced from 1024 Mbps to 450 Mbps due to the misalignment between the Tx and Rx horns. By introducing the transmissive RIS and scanning the beam it forms to the 30° direction, the maximum 1683 Mbps data rate is achieved. As a result, we can conclude that the transmissive RIS is able to dynamically steer its beam to adapt to the variation of the incident angle of the signal. Similar to the experiment in the previous subsection, the obstacle is again introduced into the communication prototype. The experiment results validate that the transmissive RIS is able to improve the data rate and overcome obstacles at an oblique incident angle $\theta_t = 30°$.

VI. CONCLUSION

The transmissive RIS has a promising prospect in B5G communications to provide enhanced signal coverage in various communication scenarios. Compared to the reflective RIS, the research and experimental demonstration of the transmissive RIS and the transmissive RIS-aided communication system are considerably fewer. This work proposes a novel 2-bit transmissive RIS design with a 90° digital phase shifter and a 1-bit vertical current reversible dipole. The 2-bit phase controlling capability is achieved and measured. Experimental results show the transmissive RIS prototype with 16×16 elements can provide a broadside gain of 22.0 dBi at 27.0 GHz. Moreover, a transmissive RIS-aided communication prototype is set up, and the system performances for three representative scenarios are measured. It is experimentally demonstrated that the transmissive RIS is able to achieve higher data rate, reduce the transmit power, improve the transmission capability through obstacles, and dynamically adapt to the signal propagation direction.

APPENDIX A

The upper bound of (4) is given by $\text{SNR} \leq \frac{P_t G F \lambda^2 \Gamma^2}{16\pi^2\sigma^2}\left(\sum_{m=0}^{N_x-1}\sum_{n=0}^{N_y-1}\left|\frac{1}{d^t_{m,n}d^r_{m,n}}\right|\right)^2$. Notice that when $\phi_{m,n} = \frac{d^t_{m,n}+d^r_{m,n}}{\lambda} + C$ with C being an arbitrary constant, SNR can be rewritten as

$$\begin{aligned}\text{SNR} &= \frac{P_t G F \lambda^2 \Gamma^2}{16\pi^2\sigma^2}\left|\sum_{m=0}^{N_x-1}\sum_{n=0}^{N_y-1}\frac{1}{d^t_{m,n}d^r_{m,n}}e^{jC}\right|^2 \\ &= \frac{P_t G F \lambda^2 \Gamma^2}{16\pi^2\sigma^2}\left(\sum_{m=0}^{N_x-1}\sum_{n=0}^{N_y-1}\left|\frac{1}{d^t_{m,n}d^r_{m,n}}\right|\right)^2, \end{aligned} \quad (12)$$

where the upper bound is achieved. Therefore, the phase shift $\phi_{m,n} = \frac{d^t_{m,n}+d^r_{m,n}}{\lambda} + C$ can maximize the SNR. Finally, due to the 2π period of the function e^{jx}, i.e., $e^{jx} = e^{j(x+2k\pi)}, k \in \mathbb{Z}$, we can conclude that $\bar{\phi}_{m,n} = \text{mod}\left(\frac{d^t_{m,n}+d^r_{m,n}}{\lambda} + C, 2\pi\right)$ is also the maximizer to SNR.

REFERENCES

[1] J. Tang, S. Xu, and F. Yang, "Design of a 2.5-D 2-bit reconfigurable transmitarray element for 5G mmWave applications," in *Proc. IEEE Int. Symp. Antennas Propag.*, Jun. 2020, pp. 631–632.

[2] F. E. Idachaba, "5G networks: Open network architecture and densification strategies for beyond 1000x network capacity increase," in *Proc. Future Technol. Conf. (FTC)*, Dec. 2016, pp. 1265–1269.

[3] T. S. Rappaport et al., "Wireless communications and applications above 100 GHz: Opportunities and challenges for 6G and beyond," *IEEE Access*, vol. 7, pp. 78729–78757, 2019.

[4] W. Tang et al., "Wireless communications with reconfigurable intelligent surface: Path loss modeling and experimental measurement," *IEEE Trans. Wireless Commun.*, vol. 20, no. 1, pp. 421–439, Jan. 2021.

[5] P. Wang, J. Fang, X. Yuan, Z. Chen, and H. Li, "Intelligent reflecting surface-assisted millimeter wave communications: Joint active and passive precoding design," *IEEE Trans. Veh. Technol.*, vol. 69, no. 12, pp. 14960–14973, Dec. 2020.

[6] C. Huang, A. Zappone, G. C. Alexandropoulos, M. Debbah, and C. Yuen, "Reconfigurable intelligent surfaces for energy efficiency in wireless communication," *IEEE Trans. Wireless Commun.*, vol. 18, no. 8, pp. 4157–4170, Aug. 2019.

[7] L. Dai et al., "Reconfigurable intelligent surface-based wireless communications: Antenna design, prototyping, and experimental results," *IEEE Access*, vol. 8, pp. 45913–45923, 2020.

[8] L. Wei et al., "Multi-user holographic MIMO surfaces: Channel modeling and spectral efficiency analysis," *IEEE J. Sel. Topics Signal Process.*, vol. 16, no. 5, pp. 1112–1124, Aug. 2022.

[9] Y. Wang, G. Wang, R. He, B. Ai, and C. Tellambura, "Doppler shift and channel estimation for intelligent transparent surface assisted communication systems on high-speed railways," *IEEE Trans. Commun.*, early access, May 12, 2023, doi: 10.1109/TCOMM.2023.3275590.

[10] (2020). *DOCOMO Conducts World's First Successful Trial of Transparent Dynamic Metasurface*. Accessed: Jan. 17, 2020. [Online]. Available: https://www.docomo.ne.jp/english/info/media_center/pr/2020/0117_00.html

[11] M. Sazegar et al., "Beam steering transmitarray using tunable frequency selective surface with integrated ferroelectric varactors," *IEEE Trans. Antennas Propag.*, vol. 60, no. 12, pp. 5690–5699, Dec. 2012.

[12] L. Boccia, I. Russo, G. Amendola, and G. Di Massa, "Multilayer antenna-filter antenna for beam-steering transmit-array applications," *IEEE Trans. Microw. Theory Techn.*, vol. 60, no. 7, pp. 2287–2300, Jul. 2012.

[13] J. Y. Lau and S. V. Hum, "Analysis and characterization of a multipole reconfigurable transmitarray element," *IEEE Trans. Antennas Propag.*, vol. 59, no. 1, pp. 70–79, Jan. 2011.

[14] W. Pan, C. Huang, X. Ma, and X. Luo, "An amplifying tunable transmitarray element," *IEEE Antennas Wireless Propag. Lett.*, vol. 13, pp. 702–705, 2014.

[15] J. Y. Lau and S. V. Hum, "Reconfigurable transmitarray design approaches for beamforming applications," *IEEE Trans. Antennas Propag.*, vol. 60, no. 12, pp. 5679–5689, Dec. 2012.

[16] C. Huang, W. Pan, X. Ma, B. Zhao, J. Cui, and X. Luo, "Using reconfigurable transmitarray to achieve beam-steering and polarization manipulation applications," *IEEE Trans. Antennas Propag.*, vol. 63, no. 11, pp. 4801–4810, Nov. 2015.

[17] M. Frank, F. Lurz, R. Weigel, and A. Koelpin, "Electronically reconfigurable 6×6 element transmitarray at K-band based on unit cells with continuous phase range," *IEEE Antennas Wireless Propag. Lett.*, vol. 18, no. 4, pp. 796–800, Apr. 2019.

[18] A. Clemente, L. Dussopt, R. Sauleau, P. Potier, and P. Pouliguen, "1-bit reconfigurable unit cell based on PIN diodes for transmit-array applications in X-band," *IEEE Trans. Antennas Propag.*, vol. 60, no. 5, pp. 2260–2269, May 2012.

[19] W. Pan, C. Huang, X. Ma, B. Jiang, and X. Luo, "A dual linearly polarized transmitarray element with 1-bit phase resolution in X-band," *IEEE Antennas Wireless Propag. Lett.*, vol. 14, pp. 167–170, 2015.

[20] L. Di Palma, A. Clemente, L. Dussopt, R. Sauleau, P. Potier, and P. Pouliguen, "Circularly-polarized reconfigurable transmitarray in Ka-band with beam scanning and polarization switching capabilities," *IEEE Trans. Antennas Propag.*, vol. 65, no. 2, pp. 529–540, Feb. 2017.

[21] B. D. Nguyen and C. Pichot, "Unit-cell loaded with PIN diodes for 1-bit linearly polarized reconfigurable transmitarrays," *IEEE Antennas Wireless Propag. Lett.*, vol. 18, no. 1, pp. 98–102, Jan. 2019.

[22] M. Wang, S. Xu, F. Yang, and M. Li, "A 1-bit bidirectional reconfigurable transmit-reflect-array using a single-layer slot element with PIN diodes," *IEEE Trans. Antennas Propag.*, vol. 67, no. 9, pp. 6205–6210, Sep. 2019.

[23] L. Di Palma, A. Clemente, L. Dussopt, R. Sauleau, P. Potier, and P. Pouliguen, "Experimental characterization of a circularly polarized 1 bit unit cell for beam steerable transmitarrays at Ka-band," *IEEE Trans. Antennas Propag.*, vol. 67, no. 2, pp. 1300–1305, Feb. 2019.

[24] Y. Wang, S. Xu, F. Yang, and D. H. Werner, "1 bit dual-linear polarized reconfigurable transmitarray antenna using asymmetric dipole elements with parasitic bypass dipoles," *IEEE Trans. Antennas Propag.*, vol. 69, no. 2, pp. 1188–1192, Feb. 2021.

[25] C. Luo, G. Zhao, Y. Jiao, G. Chen, and Y. Yan, "Wideband 1 bit reconfigurable transmitarray antenna based on polarization rotation element," *IEEE Antennas Wireless Propag. Lett.*, vol. 20, no. 5, pp. 798–802, May 2021.

[26] A. Clemente, L. Dussopt, R. Sauleau, P. Potier, and P. Pouliguen, "Wideband 400-element electronically reconfigurable transmitarray in X band," *IEEE Trans. Antennas Propag.*, vol. 61, no. 10, pp. 5017–5027, Oct. 2013.

[27] C.-C. Cheng, B. Lakshminarayanan, and A. Abbaspour-Tamijani, "A programmable lens-array antenna with monolithically integrated MEMS switches," *IEEE Trans. Microw. Theory Techn.*, vol. 57, no. 8, pp. 1874–1884, Aug. 2009.

[28] F. Diaby, A. Clemente, R. Sauleau, K. T. Pham, and L. Dussopt, "2 bit reconfigurable unit-cell and electronically steerable transmitarray at Ka-band," *IEEE Trans. Antennas Propag.*, vol. 68, no. 6, pp. 5003–5008, Jun. 2020.

[29] B. Wu, A. Sutinjo, M. E. Potter, and M. Okoniewski, "On the selection of the number of bits to control a dynamic digital MEMS reflectarray," *IEEE Antennas Wireless Propag. Lett.*, vol. 7, pp. 183–186, 2008.

[30] H. Yang et al., "A study of phase quantization effects for reconfigurable reflectarray antennas," *IEEE Antennas Wireless Propag. Lett.*, vol. 16, pp. 302–305, 2017.

[31] Q. Wu and R. Zhang, "Beamforming optimization for wireless network aided by intelligent reflecting surface with discrete phase shifts," *IEEE Trans. Commun.*, vol. 68, no. 3, pp. 1838–1851, Mar. 2020.

[32] Y. Xiao, F. Yang, S. Xu, M. Li, K. Zhu, and H. Sun, "Design and implementation of a wideband 1-bit transmitarray based on a Yagi–Vivaldi unit cell," *IEEE Trans. Antennas Propag.*, vol. 69, no. 7, pp. 4229–4234, Jul. 2021.

[33] T. Lambard, O. Lafond, M. Himdi, H. Jeuland, and S. Bolioli, "A novel analog 360° phase shifter design in Ku and Ka bands," in *Proc. 4th Eur. Conf. Antennas Propag. (EuCAP)*, 2010, pp. 1–4.

[34] L. Wei, C. Huang, G. C. Alexandropoulos, C. Yuen, Z. Zhang, and M. Debbah, "Channel estimation for RIS-empowered multi-user MISO wireless communications," *IEEE Trans. Commun.*, vol. 69, no. 6, pp. 4144–4157, Jun. 2021.

[35] P. Wang, J. Fang, H. Duan, and H. Li, "Compressed channel estimation for intelligent reflecting surface-assisted millimeter wave systems," *IEEE Signal Process. Lett.*, vol. 27, pp. 905–909, 2020.

[36] P. Wang, J. Fang, W. Zhang, Z. Chen, H. Li, and W. Zhang, "Beam training and alignment for RIS-assisted millimeter-wave systems: State of the art and beyond," *IEEE Wireless Commun.*, vol. 29, no. 6, pp. 64–71, Dec. 2022.

[37] X. Gao, L. Dai, Y. Sun, S. Han, and I. Chih-Lin, "Machine learning inspired energy-efficient hybrid precoding for mmWave massive MIMO systems," in *Proc. IEEE Int. Conf. Commun. (ICC)*, May 2017, pp. 1–6.

[38] K.-H. Han and J.-H. Kim, "Quantum-inspired evolutionary algorithm for a class of combinatorial optimization," *IEEE Trans. Evol. Comput.*, vol. 6, no. 6, pp. 580–593, Dec. 2002.

[39] Q. Wu and R. Zhang, "Beamforming optimization for intelligent reflecting surface with discrete phase shifts," in *Proc. IEEE Int. Conf. Acoust., Speech Signal Process. (ICASSP)*, May 2019, pp. 7830–7833.

[40] S. X. Ta, H. Choo, and I. Park, "Broadband printed-dipole antenna and its arrays for 5G applications," *IEEE Antennas Wireless Propag. Lett.*, vol. 16, pp. 2183–2186, 2017.

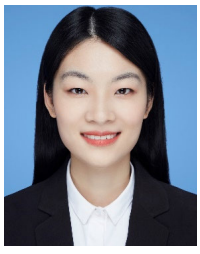

Junwen Tang received the B.S. degree in electronic information engineering from Xidian University, Xi'an, China, in 2017, and the Ph.D. degree in electronic engineering from Tsinghua University, Beijing, China, in 2022. Since 2022, she has been with the Aerospace Information Research Institute, Chinese Academy of Sciences, Beijing. Her research interests include transmitarray, reconfigurable antenna, and phased array antenna.

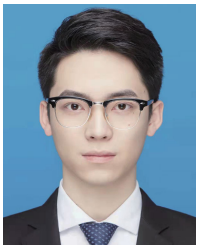

Mingyao Cui received the B.E. and M.S. degrees in electronic engineering from Tsinghua University, Beijing, China, in 2020 and 2023, respectively. His research interests include massive MIMO, millimeter-wave communications, near-field communications, and artificial intelligence empowered communications. He received the IEEE ICC Outstanding Demo Award and the National Scholarship in 2022.

Shenheng Xu (Member, IEEE) received the B.S. and M.S. degrees from Southeast University, Nanjing, China, in 2001 and 2004, respectively, and the Ph.D. degree in electrical engineering from the University of California, Los Angeles (UCLA), Los Angeles, CA, USA, in 2009.

From 2000 to 2004, he was a Research Assistant with the State Key Laboratory of Millimeter Waves, Southeast University. From 2004 to 2011, he was a Graduate Student Researcher and later a Post-Doctoral Researcher with the Antenna Research, Analysis, and Measurement Laboratory, UCLA. In 2012, he joined the Department of Electronic Engineering, Tsinghua University, Beijing, China, as an Associate Professor. His research interests include novel designs of high-gain antennas for advanced applications, artificial electromagnetic structures, and electromagnetic and antenna theories.

Linglong Dai (Fellow, IEEE) received the B.S. degree from Zhejiang University, Hangzhou, China, in 2003, the M.S. degree from the China Academy of Telecommunications Technology, Beijing, China, in 2006, and the Ph.D. degree from Tsinghua University, Beijing, in 2011.

From 2011 to 2013, he was a Post-Doctoral Researcher with the Department of Electronic Engineering, Tsinghua University, where he was an Assistant Professor from 2013 to 2016 and an Associate Professor from 2016 to 2022. Since 2022, he has been a Professor with the Department of Electronic Engineering, Tsinghua University. He has coauthored the book *MmWave Massive MIMO: A Paradigm for 5G* (Academic Press, 2016). He has authored or coauthored more than 70 IEEE journal articles and more than 40 IEEE conference papers. He holds 19 granted patents. His current research interests include massive MIMO, reconfigurable intelligent surface (RIS), millimeter-wave and terahertz communications, wireless AI, and electromagnetic information theory.

Dr. Dai was elevated as an IEEE Fellow in 2022. He received the five IEEE Best Paper Awards from the IEEE ICC and IEEE VTC. He received the Tsinghua University Outstanding Ph.D. Graduate Award in 2011, the Beijing Excellent Doctoral Dissertation Award in 2012, the China National Excellent Doctoral Dissertation Nomination Award in 2013, the URSI Young Scientist Award in 2014, the IEEE TRANSACTIONS ON BROADCASTING Best Paper Award in 2015, the *Electronics Letters* Best Paper Award in 2016, the National Natural Science Foundation of China for Outstanding Young Scholars in 2017, the IEEE ComSoc Asia–Pacific Outstanding Young Researcher Award in 2017, the IEEE ComSoc Asia–Pacific Outstanding Paper Award in 2018, the China Communications Best Paper Award in 2019, the IEEE ACCESS Best Multimedia Award in 2020, the IEEE Communications Society Leonard G. Abraham Prize in 2020, the IEEE ComSoc Stephen O. Rice Prize in 2022, and the IEEE ICC Best Demo Award in 2022. He was listed as a Highly Cited Researcher by Clarivate Analytics from 2020 to 2022. He served as an Editor for the IEEE TRANSACTIONS ON COMMUNICATIONS from 2017 to 2021, an Editor for the IEEE TRANSACTIONS ON VEHICULAR TECHNOLOGY from 2016 to 2020, and an Editor for the IEEE COMMUNICATIONS LETTERS from 2016 to 2020. He served as a Guest Editor for the IEEE JOURNAL ON SELECTED AREAS IN COMMUNICATIONS, IEEE JOURNAL OF SELECTED TOPICS IN SIGNAL PROCESSING, and IEEE WIRELESS COMMUNICATIONS. He is serving as an Area Editor for the IEEE COMMUNICATIONS LETTERS and an Editor for the IEEE TRANSACTIONS ON WIRELESS COMMUNICATIONS. Particularly, he is dedicated to reproducible research and has made a large amount of simulation codes publicly available.

Fan Yang (Fellow, IEEE) received the B.S. and M.S. degrees from Tsinghua University, Beijing, China, in 1997 and 1999, respectively, and the Ph.D. degree from the University of California, Los Angeles (UCLA), Los Angeles, CA, USA, in 2002.

From 1994 to 1999, he was a Research Assistant with the State Key Laboratory of Microwave and Digital Communications, Tsinghua University. From 1999 to 2002, he was a Graduate Student Researcher with the Antenna Laboratory, UCLA. From 2002 to 2004, he was a Post-Doctoral Research Engineer and a Instructor with the Electrical Engineering Department, UCLA. In 2004, he joined the Electrical Engineering Department, The University of Mississippi, Oxford, MS, USA, as an Assistant Professor, and was promoted to an Associate Professor in 2009. In 2011, he joined the Electronic Engineering Department, Tsinghua University, as a Professor, and served as the Director of the Microwave and Antenna Institute until 2020. He has published more than 500 journal articles and conference papers, eight book chapters, and six books entitled *Surface Electromagnetics* (Cambridge University Press, 2019), *Reflectarray Antennas: Theory, Designs, and Applications* (IEEE-Wiley, 2018), *Analysis and Design of Transmitarray Antennas* (Morgan and Claypool, 2017), *Scattering Analysis of Periodic Structures Using Finite-Difference Time-Domain Method* (Morgan and Claypool, 2012), *Electromagnetic Band Gap Structures in Antenna Engineering* (Cambridge University Press, 2009), and *Electromagnetics and Antenna Optimization Using Taguchi's Method* (Morgan and Claypool, 2007). His research interests include antennas, surface electromagnetics, computational electromagnetics, and applied electromagnetic systems.

Dr. Yang is an ACES Fellow. He was a recipient of several prestigious awards and recognitions, including the Young Scientist Award of the 2005 URSI General Assembly, the 2007 International Symposium on Electromagnetic Theory, the 2008 Junior Faculty Research Award of the University of Mississippi, the 2009 inaugural IEEE Donald G. Dudley Jr. Undergraduate Teaching Award, and the 2011 Recipient of Global Experts Program of China. He was the Technical Program Committee (TPC) Chair of 2014 IEEE International Symposium on Antennas and Propagation and USNC-URSI Radio Science Meeting. He is an IEEE APS Distinguished Lecturer from 2018 to 2021. He served as an Associate Editor for the IEEE TRANSACTIONS ON ANTENNAS AND PROPAGATION from 2010 to 2013 and an Associate Editor-in-Chief for *Applied Computational Electromagnetics Society (ACES) Journal* from 2008 to 2014.

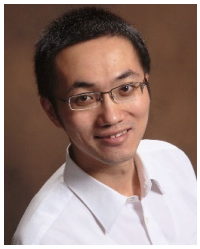

Maokun Li (Senior Member, IEEE) received the B.S. degree in electronic engineering from Tsinghua University, Beijing, China, in 2002, and the M.S. and Ph.D. degrees in electrical engineering from the University of Illinois Urbana-Champaign, Champaign, IL, USA, in 2004 and 2007, respectively. After graduation, he was a Senior Research Scientist with the Schlumberger-Doll Research, Cambridge, MA, USA. In 2014, he joined the Department of Electronic Engineering, Tsinghua University, Beijing. His research interests include fast algorithms in computational electromagnetics and their applications in antenna modeling, electromagnetic compatibility analysis, geophysical exploration, and biomedical imaging. He was among a recipients of the 2017 IEEE Ulrich L. Rohde Innovative Conference Paper Award and the 2019 PIERS Young Scientist Award. He serves as an Associate Editor for IEEE TRANSACTIONS ON ANTENNAS AND PROPAGATION and IEEE TRANSACTIONS ON GEOSCIENCE AND REMOTE SENSING.